Coupling Diffraction Contrast Tomography with the Finite Element Method**

By *Henry Proudhon,* Jia Li, Peter Reischig, Nicolas Guéninchault, Samuel Forest* and *Wolfgang Ludwig*

In this paper explains how to turn full three dimensional (3D) experimental grain maps into a finite elements (FE) mesh suitable for mechanical analysis. Two examples from diffraction contrast tomography characterizations are presented. Deformation of a pure titanium sample with 1400 grains is computed using elastic anisotropy and accurate boundary conditions allows to correctly capture the grain to grain elastic strain variations. In the second example a significantly large zone of a polycrystalline Al–Li sample is meshed and computed using elastoplastic finite strain calculation. Mean lattice reorientations and intra-grain lattice orientation spread are obtained as a function of deformation.

1. Introduction

Continuum crystal plasticity has proved to be a powerful tool to interpret experimental results obtained in the deformation of metallic polycrystals.[1] Large scale simulations on polycrystalline volume elements can now be performed with sufficient local discretization to predict the transgranular plastic strain fields. They are necessary for comparison with results of sophisticated 2D and 3D full field measurements providing strain fields based on grid methods and/or image correlation techniques,[2] lattice rotation fields by means of Electron Back Scattered Diffraction (EBSD),[3,4,5] elastic strain fields using for instance micro-diffraction techniques.[6]

Even though continuum crystal plasticity constitutive equations do not account for the intricate dislocation mechanisms at work during plastic deformation, the continuum mechanical model gives relevant information about the strain heterogeneities induced in a polycrystal by the strong incompatibilities that develop at grain boundaries. These predictions are based on the precise kinematic description of the crystallographic nature of plastic slip in grains. For that purpose, full 3D simulations are necessary even when only 2D measurement information is available, due to the 3D nature of multislip mechanisms. Some of the first illustrations of the tremendous heterogeneities that develop in polycrystals were provided in refs.[7,8,9]

In the last 10 years, Synchrotron X-ray diffraction using fast 2D imaging detectors have made tremendous progress. Both Diffraction Contrast tomography (DCT) and High Energy Diffraction Microscopy (HEDM) can now provide complete three-dimensional reconstruction of the grain microstructure of millimeter sized metallic samples with several thousand grains. Forward modeling methods can now be used to extract local intragranular lattice rotations in each of the reconstructed grain.[10,11] This will probably be one of the key features used in the future to analyze material deformation mechanisms and degradation. Serial sectioning techniques are also heavily developing such as FIB/EBSD imaging and femtosecond laser ablation techniques coupled to EBSD (TriBeam experiments).[12]

All these new experimental developments can provide 3D microstructure images to serve as input for finite element calculations of the local/global mechanical properties.

2. 3D Mesh Generation from Tomographic Images

Microstructural description of polycrystalline (or multiphase) materials are generally described by digital images

[*] Dr. H. Proudhon, Dr. J. Li, Dr. N. Guéninchault, Dr. S. Forest
MINES ParisTech, PSL Research University, MAT – Centre des matériaux, CNRS UMR 7633, BP 87 91003, Evry, France
E-mail: henry.proudhon@mines-paristech.fr
Dr. P. Reischig
Xnovo Technology ApS, 4600, Koege, Denmark
Dr. P. Reischig, Dr. W. Ludwig
MATEIS, INSA de Lyon, Villeurbanne 69621, France
Dr. W. Ludwig
European Synchrotron Radiation Facility, Grenoble, 38043, France

(could be 2D or 3D) composed by patches of constant positive integers called labels and representing the different phases. When meshing a multi-labeled image, two radically different approaches are generally considered: i) voxel-based meshing using hexahedra; ii) free meshing using tetrahedra. Free meshing using hexahedra also exist and may play an important role in the future due to the better numerical precision achieved by those elements in comparison to tetrahedra but algorithms are still under development.[13]

Choosing between meshing methods usually depends on the goal to achieve but it can be observed that when working in 3D, and depending of the spatial resolution, voxel-based meshing may lead to prohibitive computational cost. Let us take a cubic grain of size $d = 50\,\mu m$. For voxel-based meshing, the number of elements can readily be calculated as $(d/a)^3$, with a the element size at the grain boundary. For free meshing with tetrahedron, a geometric progression of the element size can be used with coarser elements at the center of the grain, for this value of q. For a progression $q > 1$ the total number of elements can be approximated by $6(d/a)^2 \times 2n$; n being the number of elements from the grain boundary to the middle of the grain. The factor 6 comes from the regular division of a cube into 6 tetrahedra. n is, thus, linked to half the grain size by $n = a + qa + \cdots + q^{n-1} = a(1 - q^n)/(1 - q) = d/2$, and can be calculated by $n = log(1 + (q - 1)d/2a)/log(q) \propto log(d/a)$. Finally, the total number of elements scales in $(d/a)^2\,log(d/a)$ instead of $(d/a)^3$. Table 1 compares the number of elements required to mesh our $50\,\mu m$ grain with a progression of $q = 2$ and different spatial resolutions. If one relaxes the constraint of having a constant spatial resolution at the grain boundary but only at the edges of the grain boundaries (triple lines), the comparison is even more in favor of free meshing since it now scales like $[log(d/a)]^3$. Indeed with the same kind of arguments, the element size is a at the edges of the grain boundary and increases to aq^{n-1} at the center of the grain boundary with $n \propto log(d/a)$. So the number of elements on the grain boundary scales like $[log(d/a)]^2$ and the total number of element in the grain scales like $[log(d/a)]^3$.

Modern meshing software now allow to control the mesh density using a metric based on the proximity of features and this is typically what should be used to produce a high fidelity mesh of a multi-labeled image with the constraint of a reasonable number of elements (which can still reach several millions).

Table 1. Comparison of the number of elements required to mesh a $50\,\mu m$ grain with an element size equal to a at the grain boundary, between voxel-based and free meshing with a progression of $q = 2$.

a [μm]	Voxel-based meshing	Free meshing
1.0	125 k	150 k
0.5	1 000 k	720 k
0.2	15 625 k	5 250 k
0.1	125 000 k	24 000 k

2.1. Voxel-Based Meshing of Multi Labeled Images

Voxel-based meshing consists in building a regular mesh of the size of the image and then grouping elements corresponding to each grain into element sets. The grain orientation can the n be assigned to each particular set.

Two examples are presented here to illustrate this method. The first example is a Ni-based superalloy imaged by EBSD with a $1\,\mu m$ step size (see Figure 1). The meshing was done directly as this resolution with an element size of $1\,\mu m$. After fitting a non-linear crystal plasticity behavior to the macroscopic stress/strain curve, an average axial strain of 1% was applied using a generalized plan strain formulation to assess the heterogeneous stress distribution within the grains, see Figure 1c.

In the second example, a 316LN stainless steel sample imaged by EBSD via serial sectioning (courtesy Th. Ghidossi and L. Signor at Pprime institute, see ref.[14] for more details) is meshed. The grain aggregate is fitted with a crystal plasticity behavior[15] and fatigue cycles are computed to try to reproduce the experimentally observed fatigue crack initiation locations (see Figure 2). The image data have been down sampled by a factor of 4 in both x and y directions to limit the number of elements below 1 million to be able to compute several fatigue cycles with a non-linear crystal plasticity behavior in a few days.

In summary, voxel-based meshing is fast and remains easy to implement. It has, however, two major drawbacks: it produces staircase like grain boundaries due to the regular mesh and the number of elements scales very rapidly with the spatial resolution. This type of discretization (although not really meshed) is used for FFT-based mechanical calculations[16] and the argument holds true also in that case.

Voxel-based meshing may also be useful when considering grain microstructure with non-uniform orientation by grain. In this case, the orientation needs to be specified on a per element basis and a voxel-based mesh may be the more convenient way to achieve that, but up to now this remains largely unexplored.

2.2. Free Meshing of Multi Labeled Images

The construction of a realistic mesh with tetrahedra finite elements from a multi-labeled tomographic image representing a polycrystalline microstructure is a non-trivial procedure.

In the simplest case, the microstructure image is composed by only one slice (surface EBSD for instance). This is the case for instance of thin polycrystalline films which exhibit a columnar grain structure in the film thickness direction. An example of a mesh reconstructed by surface observation of a 400 nm thick gold film with an in-plane grain size of $1\,\mu m$ is shown in Figure 3. This work was done in collaboration with S. Labat (IM2NP, Marseille). In this particular case, the EBSD mapping was not precise enough to mesh directly from its data. An SEM image in backscattered contrast was used, the grain boundaries isolated by image analysis and skeletonized to form the grain map and produce the free mesh with 407 grains. Then the EBSD data was used to assign the
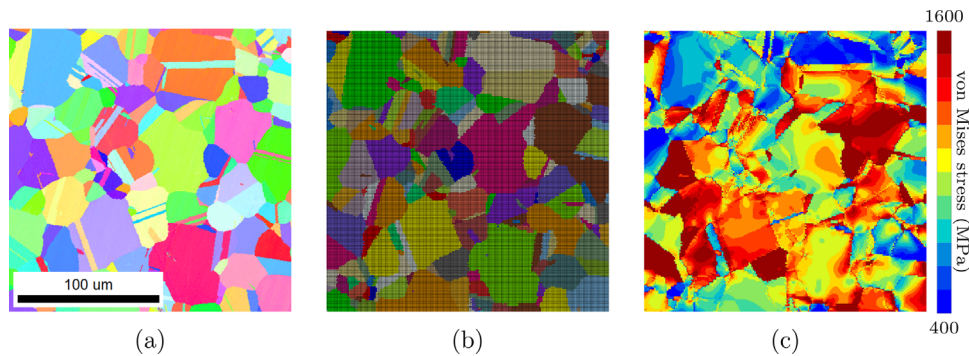
Fig. 1. (a) EBSD mapping of a Nickel-based supperalloy sample (IPF coloring); (b) voxel-based meshing of the corresponding area ($200 \times 200\,\mu m^2$); (c) von Mises stress distribution after 1% axial strain.

orientation of the 234 grains present in the mapping based on the center of mass of the grains. The other 173 grain orientations were randomly selected in agreement with the film texture. Finally, the 2D mesh was extruded on a 400 nm depth to form the 3D polycrystalline film and can be used to study numerically coherent diffraction patterns as in ref.[17]

The general case of a real 3D microstructure is much more challenging. Recent progress with various 3D imaging techniques of polycrystalline microstructures triggered new software developments to handle such images. One can cite the open source DREAM3D software developed by[19] or commercial suites like Avizo[20] or Simpleware.[21]

New methods have been recently published and may greatly ease this process although not yet readily available. F. N'Guyen uses an original approach purely based on morphological mathematics to mesh multi-phased structures without any ambiguity.[22] With a completely different philosophy, level set functions coupled to anisotropic remeshing can be used to obtain a high fidelity mesh of any 3D image.[23] This method is currently applied on 3D images based on Laguerre tessellations to study recrystallization.[24,25] The last approach that is worth mentioning is the one carried out by R. Quey and implemented in its open source software Neper.[26] Beside the usual voxel-based and Voronoï tesselation meshing, Neper can also be used to tweak a tessellation based on the center of mass of the grains to mimic the experimental microstructure.

In the present work, the meshing strategy consists of three main steps: surface mesh generation of the grain boundaries, simplification, and filling the surface mesh with tetrahedral
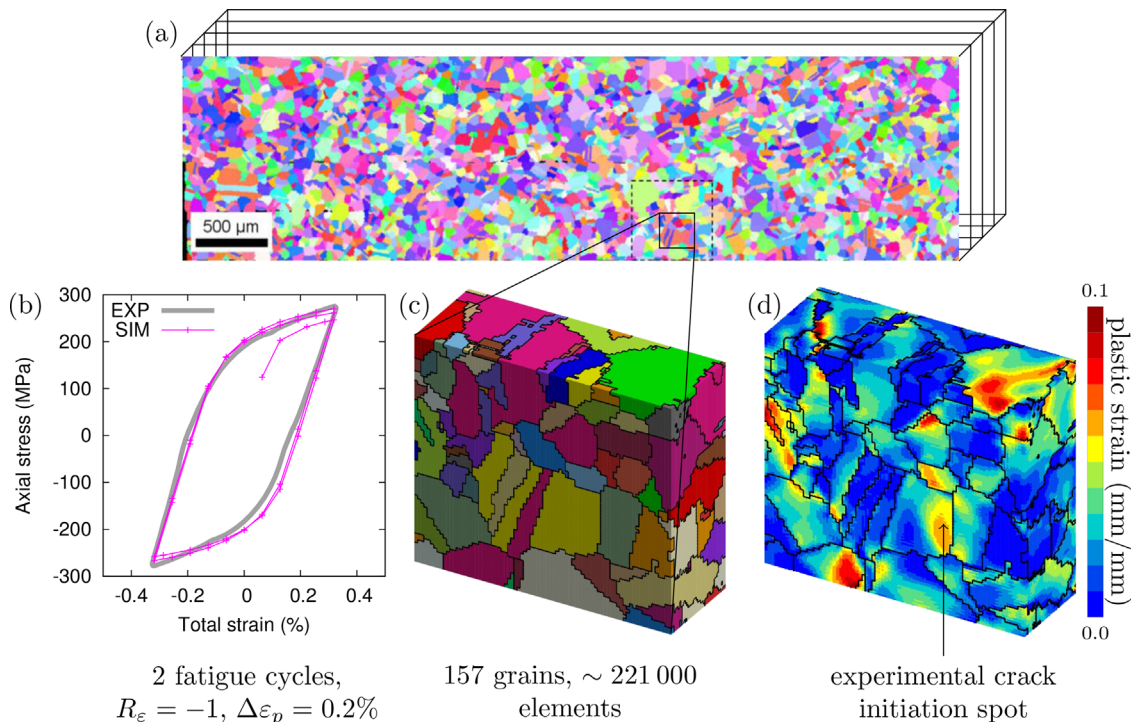

2 fatigue cycles,
$R_\varepsilon = -1$, $\Delta\varepsilon_p = 0.2\%$

157 grains, $\sim 221\,000$ elements

experimental crack initiation spot

Fig. 2. (a) Serial sectioning EBSD mappings of a 316LN sample after 5 000 fatigue cycles, the total volume analyzed was $5.0 \times 1.5 \times 0.127\,mm^3$ with several 10 thousands grains and 41 surface cracks (courtesy L. Signor, P' institute); (b) comparison of the stress/strain curve measured and simulated on the grain aggregate (c) voxel-based 157 grain aggregate meshed from the EBSD data; (d) accumulated plastic strain after the second fatigue cycle showing some of the hot spots observed experimentally.

(b) BS e- contrast

(a) EBSD IPF
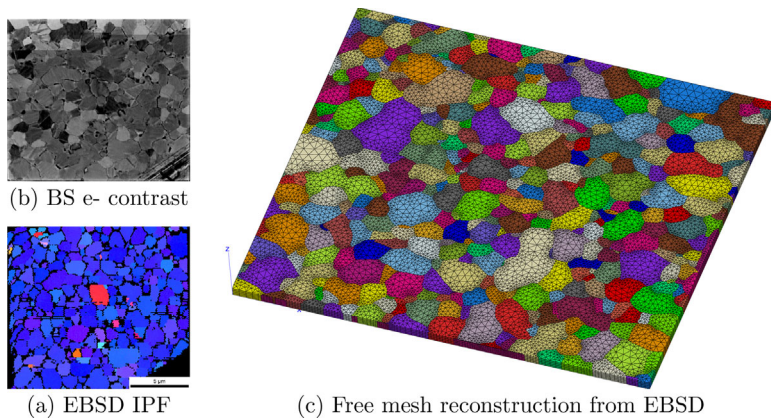
(c) Free mesh reconstruction from EBSD

Fig. 3. (a) Scanning electron micrograph used to find the grain boundaries; (b) EBSD mapping of the film surface, IPF coloring; (c) free meshing of the gold film used for coherent diffraction imaging simulations, see ref.[18] for the experimental study.

volume elements. Finally, a 3D FE mesh with a high fidelity with respect to the polycrystalline sample is obtained.

2.2.1. Surface Mesh Generation

The 3D grain boundary surface mesh is typically generated by a multiple material marching cubes algorithm[27] applied to a segmented image to generate a triangulated surface mesh. Subsequent surface smoothing is carried out by a laplacian filter, this removes most of the staircase artifacts typical of marching cubes algorithms.

2.2.2. Mesh Simplification

Depending on the spatial resolution of the input 3D image, the surface mesh created at this point may contain millions of sub-voxel sized elements. Mesh coarsening is thus carried out using an iterative decimation approach by collapsing edges into vertices in a given range, which allows to preserve mesh topology.[28] Minimum and maximum edge length are to be well chosen at this point since those values directly control the mesh density on the grain boundaries in the final volumic mesh.

2.2.3. Volume Mesh Generation

Once the surface mesh of the grain boundaries is obtained, the volume mesh generator Ghs3d, developed by Inria and distributed by Distene,[29] is used. The volume mesh generation is based on the Delaunay method described in details in ref.[30] A tetrahedral mesh suitable for FE calculation and respecting the geometry of the grain boundaries is created. Finally, a mesh optimization step is performed to improve the mesh quality.

2.2.4. Relabeling Grains

The last step of the mesh generation consists in relabeling the grains in order to have the same grain label as in the tomographic images (see Figure 4a), to assign reliably the measured grain orientation to each grain of the FE mesh. For this the center of mass of each grain in the mesh is calculated from the center of mass of its elements. Then, the corresponding grain number is determined in the tomographic images and assigned to the FE mesh. This of course works only if the FE produced mesh is of high fidelity and if the grain shapes are not too tortuous, but it proved to work remarkably well for the materials investigated here.

The geometric precision in terms of grain boundary positions of the FE mesh reconstructed by this method has been analyzed showing a very good agreement between the mesh and the tomographic image (see Figure 4b). To conclude this part, a selection of meshes obtained by the present method are shown in Figure 5.

3. Example of Experimental-Numerical Comparison in a Pure Ti Sample

The pure α-titanium has a relatively low atomic number of 22 and an appropriate mass density favorable for tomographic acquisition. Typically at energy $E = 40\,keV$, the mass attenuation coefficient is $2.214\,cm^2\,g^{-1}$. Combined with a mass density of $\rho = 4.54\,g\,cm^{-3}$, the Beer–Lambert law gives a
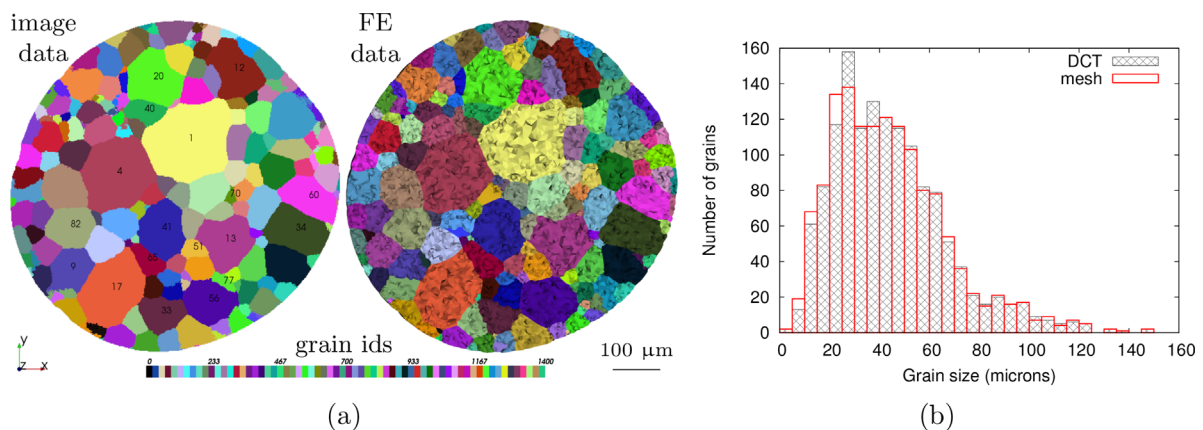

Fig. 4. (a) One horizontal slice of the tomographic images colored by grain number on the left and the corresponding slice of the FE mesh on the right; (b) comparison of 3D grain size distributions in the original DCT image and in the FE mesh (pure Ti sample, see Section 3).
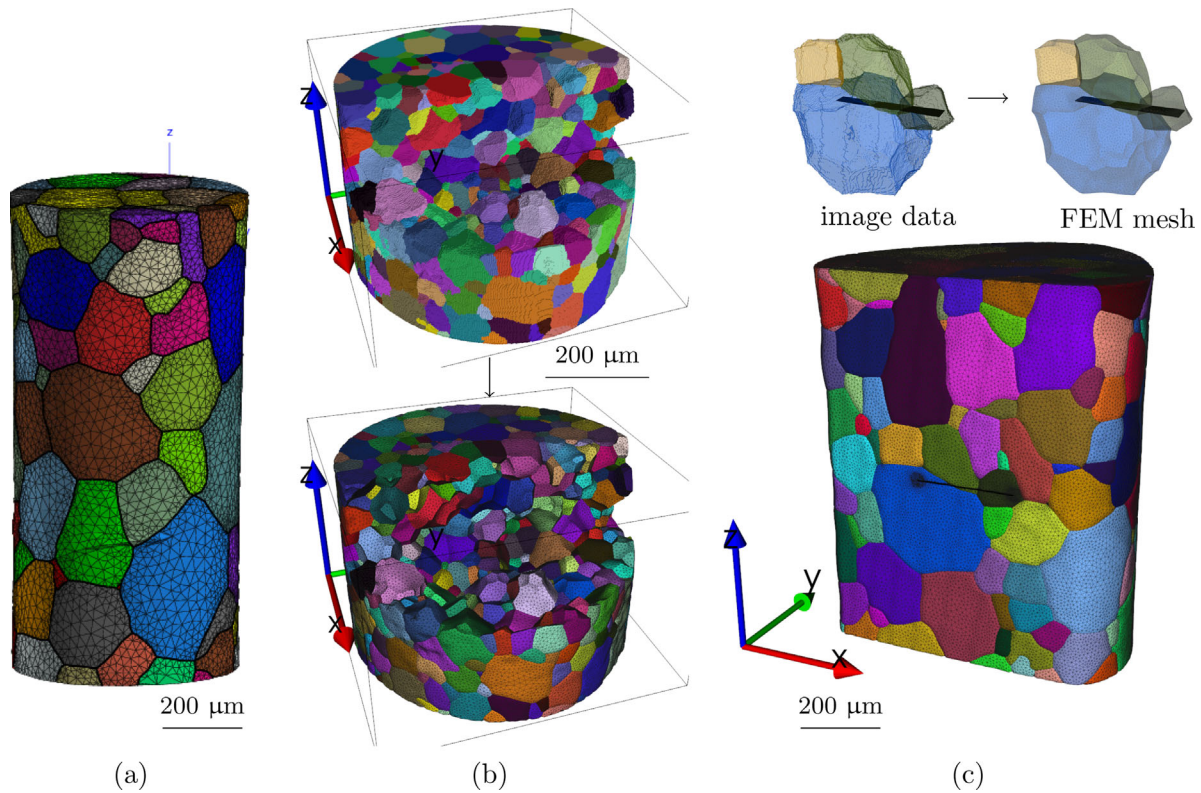
Fig. 5. (a) β-Ti 130 grains sample,[31] (b) both image data and FE mesh for the pure-Ti 1 400 grains sample (some of the grains were removed to see the interior of the sample), (c) 55 531 β-Ti sample with 387 grains and a central crack, a close up view of some of the grains of interest is shown both for image data and the corresponding FEM mesh.

transmission of 36% through a 1 mm sample and 54% through a 0.6 mm sample. It is also possible to obtain a well recrystallized microstructure with grains of around 50 μm and its elastic constants are well-known. Therefore, it has been selected to investigate the development of elastic strains within the grains both experimentally and numerically.

3.1. Elastic Behavior of Pure Titanium

Pure α-titanium has a Hexagonal Close-Packed (HCP) crystal structure which can be described by a primitive hexagonal Bravais lattice with a two point basis, one atom at (0,0,0) and another at (2/3,1/3,1/2). The lattice parameters are $a = 0.295$ nm and $c = 0.468$ nm.[32] The ratio of c/a is 1.587, which is slightly below the ideal value of $\sqrt{8/3} \simeq 1.633$ for spheres close packing. Because of the hexagonal Bravais lattice, the elasticity tensor features a transversely isotropic symmetry. The elastic constants (in MPa) in Voigt's notation for pure titanium are the following:[33]

$$
\underset{\approx}{C} = \begin{pmatrix}
162000 & 92000 & 69000 & 0 & 0 & 0 \\
92000 & 162000 & 69000 & 0 & 0 & 0 \\
69000 & 69000 & 180000 & 0 & 0 & 0 \\
0 & 0 & 0 & 46700 & 0 & 0 \\
0 & 0 & 0 & 0 & 46700 & 0 \\
0 & 0 & 0 & 0 & 0 & 35000
\end{pmatrix}.
$$

(1)

The tensor of elasticity is slightly anisotropic, with the two anisotropy factors A and B related to some of the compliance tensor components s_{ij} ($\underset{\approx}{S}$ can be derived from the tensor of elastic moduli $\underset{\approx}{C}$):

$$
A \frac{s_{11}}{s_{33}} = 1.39,
$$

(2)

$$
B \frac{2(s_{11} - s_{13})}{s_{44}} = 1.07,
$$

(3)

Considering uniaxial loading, one can express Young's modulus for hexagonal symmetry in terms of the elastic coefficients s_{ij}:[34]

$$
\frac{1}{E(\underline{n})} = s_{11} - \left[(s_{11} - s_{33})n_3^2 + 2(s_{11} - 2s_{13} - s_{44})(n_1^2 + n_2^2) \right]n_3^2
$$

(4)

Young's modulus is maximum along the [0001] direction with a value of 142 500 MPa.

3.2. Managing Crystal Orientations and Boundary Conditions from the Experiment to the FE Calculation

The DCT experiment of the pure titanium sample was carried out at the ESRF on the ID19 beamline using a compact compression stress rig driven by a piezoelectric actuator (see ref.[35] for more details). The X-ray energy was 36 keV, the

sample was placed in the stress rig at 6 mm from the detector which had an effective pixel size of 1.5 μm. The diameter of the circular cross-section of the sample was 648 μm and the height of the illuminated zone was 423 μm. Two stages of compressive loading were recorded: one at a compressive force of −4 N and other at −29 N. After image reconstruction, 1 343 grains were reconstructed in the volume at −4 N and 1 397 grains in the volume at −29 N which was thus chosen for the creation of the FE mesh (see Section 2).

The grain orientations as determined by DCT are usually expressed via Rodrigues vectors.[36] In the Z-set FE code,[37] grain orientations are specified by the three Euler angles (ϕ_1, Φ, ϕ_2) using the convention of Bunge (Z, X, Z rotations). This conversion is applied for each grain to prescribe the experimentally measured orientation in the calculation. The FE (XYZ) coordinate system then matches the experimental coordinate system (X is the X-ray propagating direction, Z is the vertical direction). It is important to understand that both the mesh and grain orientations are to be expressed in the (XYZ) laboratory coordinate system to ensure consistency between the measurements and the calculation.

Regarding boundary conditions, first the strain measurements at −4 N showed that the deformation in some grains was already significant, of the order of 0.001. This strain can be considered as a residual strain and should not be accounted for in our comparison with FE predictions. Therefore, the calculation results were compared to the strain tensors difference $\Delta \varepsilon$ between −4 and −29 N stages.

In addition, it was observed in the DCT measurements at −29 N, that the compression was not perfectly uniaxial and that a bending load was also present due to the small misalignment between sample surfaces which were not perfectly parallel. In order to apply the corresponding Boundary Conditions (BC) in the FE simulations, a linear regression of the $\Delta \varepsilon_{33}$ at (−29 N–(−4 N)), which is −25 N along the direction of compression z was determined as a function of the coordinates (x,y) of the grain centers.For this purpose, $\Delta \varepsilon_{33}$ is integrated along the loading direction at each pixel of the top surface and then divided by its pixel number of the z-direction. A linear regression, $\Delta \varepsilon_{33}$ is then obtained:

$$\Delta \varepsilon_{33}(x, y) = -0.00044 - 0.00313x - 0.00291y, \quad (5)$$

with x and y in mm. The displacement difference at the top surface is then written as

$$\Delta U_3(x, y) = \Delta \varepsilon_{33}(x, y)H, \quad (6)$$

with H the height of the illuminated zone (here 0.423 mm).

3.3. Comparison of Elastic Strain Tensors

Since the experiment remained macroscopically elastic and only elastic strains were measured, the FE calculation was carried out using the elastic behavior detailed in 3.1. All 165 grains composing the middle slice of the volume were investigated in detail (see Figure 4a). The elastic strain tensors of grains that lie close to the top and the bottom surfaces were considered not reliable because of the effect of the applied boundary conditions and the incomplete grain shapes due to the limited height of X-ray beam. Other strain components than ε_{33} are of the order of 10^{-6} or 10^{-5}, which is below the accuracy of the measurements estimated at about $5 \times 10s^{-4}$.[35] Therefore, in the following results, only the mean $\Delta \varepsilon_{33}$ of each grain are compared.

In Figure 6, almost all values of $\Delta \varepsilon_{33}$ are distributed between −0.2% and +0.1%. On the x-axis, grains are sorted by their size: grain number 1 is the largest grain and grain number 1 400 is the smallest one. The DCT measurement is able to capture the variations of $\Delta \varepsilon_{33}$ between one grain and another. This can be observed particularly clearly around grain number 400 in Figure 6b. This variation is mainly due to the different crystal orientations between grains. The distribution of this particular strain component is shown in Figure 6. It can been seen that the calculated $\Delta \varepsilon_{33}$ distribution is very similar to the experimental measurements in Figure 6a; in particular some grains experiencing tensile load are captured (this can be explained by the bending applied by Eq. 5).

The comparison of $\Delta \varepsilon_{33}$ is plotted according to the grain size (the symbol size s proportional to the grain size) in Figure 7a. The black line along the diagonal represents the same strain value between DCT and FE elastic simulation. The black dashed lines show the ±0.0005 differences that is the precision of DCT measurement. It can be observed that the comparison for the medium-sized grains (grain numbers between 50 and 1 000) is very satisfying.
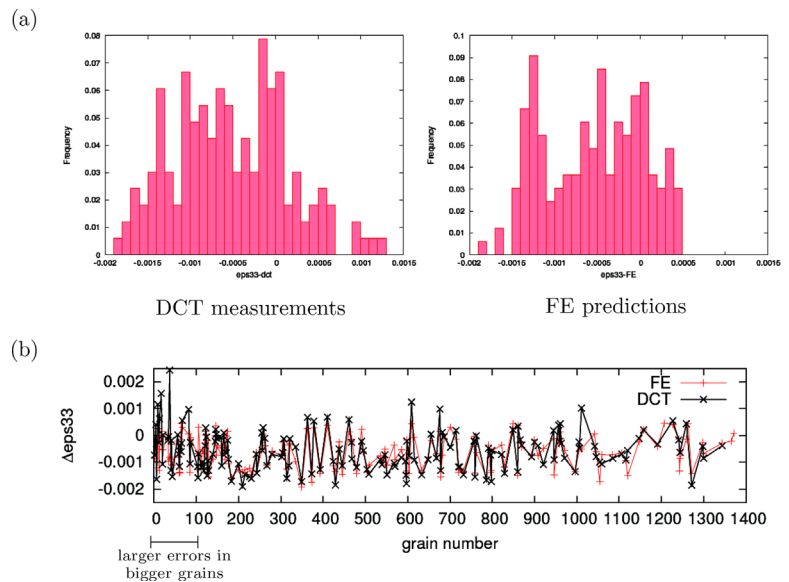
(a)

DCT measurements   FE predictions

(b)

Fig. 6. Distribution of average $\Delta \varepsilon_{33}$ in the middle slice (a) in the DCT measurements and (left) in the FE simulation (right); (b) grain-by-grain comparison between DCT measurements and FE predictions.
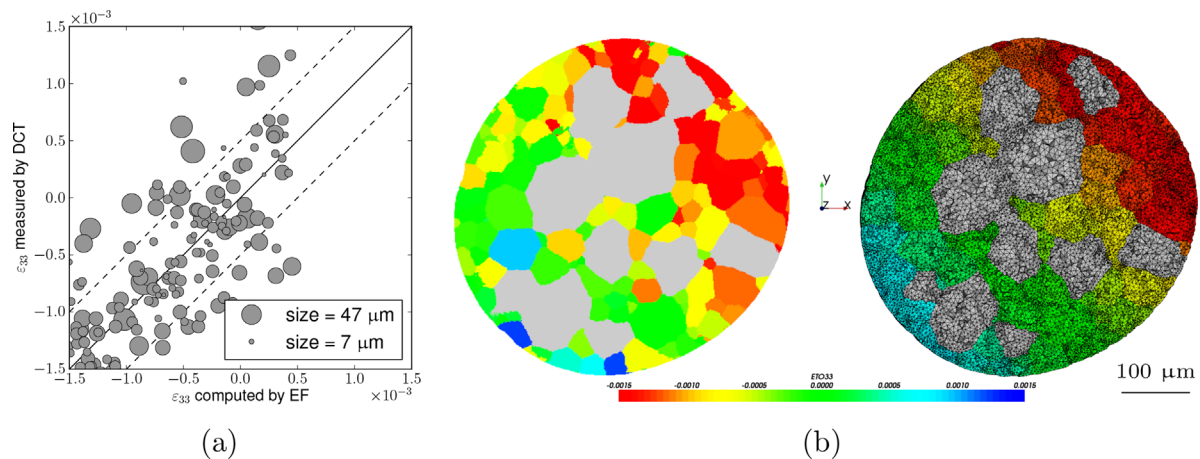
(a)

(b)

Fig. 7. (a) Comparison of the $\Delta \varepsilon_{33}$ per grain between DCT and FE simulation plotted by grain size; (b) average $\Delta \varepsilon_{33}$ per grain in the middle slice determined by DCT measurements (on the left) and by FE simulations (on the right); the big grains with numbers from 1 to 50 have been grayed out.

A visual representation of the comparison of this component is also given in Figure 7b. The grains in grey color represent the largest grains with numbers from 1 to 50. The difference between experiment and FE for medium-sized grains is generally lower than $\pm 5 \times 10^{-4}$ i.e., within the experimental uncertainty. For the small-sized grains (with numbers higher than 1 000 in Figure 6b), the DCT measurement is less accurate than that for the medium sized grains, because it is more difficult to identify all the small diffraction spots. Contrary to the small-sized grains, the diffraction spots for the big grains (grain numbers from 1 to 50) are large. However, the comparison of strain tensors of the big grains is also less accurate. This is due to a less precise determination of the center of mass of big grains in the DCT measurements, leading to their unrealistically large deformations, as shown in Figure 6b.

4. Deformation Simulation of an Al–Li Polycrystal Imaged by Diffraction Contrast Tomography

The last example is an Al–Li sample imaged by Diffraction Contrast Tomography at the ID11 beamline (ESRF). This part focus on using the experimental microstructure as input for a FE analysis to analyze the grain rotations during tension. A small tension sample with a dog-bone gage length and minimal square cross-section of $0.5 \times 0.5 \, \text{mm}^2$, was imaged at 40 keV using a regular DCT setup (1.4 effective pixel size with $2\,048 \times 2\,048$ pixels Frelon camera placed 3 mm behind the sample). The illuminated section of the sample is 0.5 mm and three different sections were imaged and merged successfully together (1.5 mm of height in total).

The free meshing procedure is rather identical to the one explained in Section 2.1.1 apart from the gradation used to reduce the number of elements. As a side note for DCT reconstruction, the use of the absorption contrast tomography volume recorded during DCT acquisition in the direct beam as a mask turned out to be essential to capture precisely the sample edges (remember the dog bone gage length).

The grain boundary mesh with triangles featured over 16 millions faces. Laplacian smoothing and decimation are applied in turn several times to reduce the number of faces. Due to the complexity of the experimental dataset, some elements may intersect during those steps making the mesh unusable for FE computations. Generally those cases have to be handled manually. Once the surface mesh has the desired density, the 3D volumic mesh can be obtained as already explained using the INRIA's meshing tools, fully integrated into the Z-set platform. Finally each grain is relabeled as in the DCT image.

Here, a three grains cluster in the center of the sample is the region of interest here of the calculation (see Figure 8). To reduce further the number of elements, a mesh gradation is applied to keep a sufficient density in and close to that three grains cluster, and a coarser mesh everywhere else. A metric map is generated using a simple linear gradation function $f(z)$, where z is measured from the chosen grain cluster (see coordinate frame in Figure 8). That gradation produced elements from 15 µm at the origin to 75 µm at the outer edges of the sample. The number of elements of the mesh was reduced from 2 millions to 300 000 and the memory requirement for the calculation is also drastically reduced to 2 Gb.

4.1. Note About Lattice Rotations

The purpose of these computations is to observe the lattice rotations occurring in the three grains cluster highlighted in Figure 8 during a tensile test with approximately 10% strain.

Regarding constitutive equations, a finite strain crystal plasticity model described in ref.[38] after the seminal work of Mandel[39] is used. The gradient of the transformation $\underset{\sim}{\mathbf{F}}$ is split into an elastic and a plastic part as $\underset{\sim}{\mathbf{F}} = \underset{\sim}{\mathbf{E}}.\underset{\sim}{\mathbf{P}}$. Using the polar decomposition, $\underset{\sim}{\mathbf{E}}$ can also be split into a rotation part and a deformation part as $\underset{\sim}{\mathbf{E}} = \underset{\sim}{\mathbf{R}}^e.\underset{\sim}{\mathbf{U}}^e$.

It should be noted that $\underset{\sim}{\mathbf{R}}^e$ is an orthogonal tensor which gives the orientation of the basis of the eigenvectors of symmetric $\underset{\sim}{\mathbf{U}}^e$ (with respect to the initial configuration which is here the initial grain orientation) and should not be
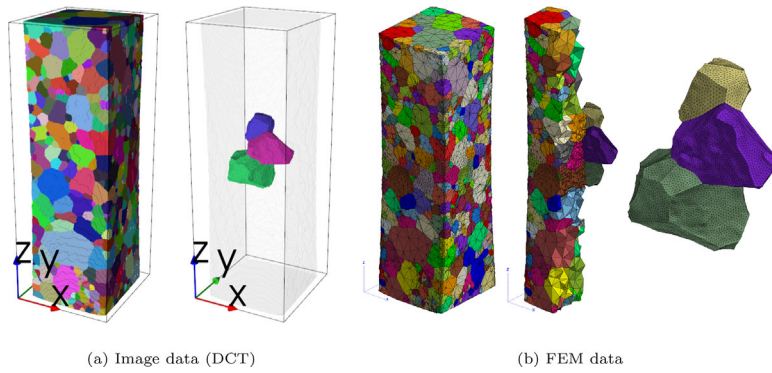
(a) Image data (DCT) (b) FEM data

Fig. 8. (a) Reconstructed microstructure of an Al–Li tension sample by DCT, with a highlight on the three grain central cluster of interest (b) free meshing of the Al–Li sample with a central mesh enrichment, ready for FEM analysis.

Table 2. Detail of the three grains investigated at the middle of the gage length.

grain id	ϕ_1	Φ	ϕ_2	Highest Schmid factor	Corresponding slip system
4	285.2	34.1	86.6	0.476	(1–11)[011]
10	262.5	16.7	86.6	0.489	(111)[011]
18	225.3	32.1	97.8	0.488	(111)[01-1]

confused with the lattice rotation. However, as soon as plasticity proceeds (typically after 0.1% but it depends on the magnitude of the elastic strains so on the material properties), the rotation of material directions included in $\mathbf{U}^e$ becomes negligible with respect to $\mathbf{R}^e$. Therefore the rotation angle $\phi_c = \arccos((tr(\mathbf{R})^e - 1/2)$, associated with $\mathbf{R}^e$ will be used to quantify the lattice rotation of the grain during the computation.

4.2. Crystal Plasticity Computation

Plastic deformation is the result of the combined slip of all the activated slip systems among the 12 octahedral slip systems: 4 {111} planes (the normal is noted $\underline{n}^s$), each one with 3 ⟨110⟩ slip directions (noted $\underline{m}^s$), so that: $\dot{\mathbf{P}} \cdot \mathbf{P}^{-1} = \sum_{s=1}^{12} \dot{\gamma}^s \underline{m}^s \otimes \underline{n}^s$. Table 2 shows the initial orientation

$(\phi_1, \mathbf{\Phi}, \phi_2)$ for the three grains of interest (the full sample does not exhibit any particular texture). The 3 Euler angles are used to define the initial lattice orientation by the orientation matrix $\mathbf{B}$. For a given slip system s, the resolved shear stress τ^s is classically expressed by the Schmid law. τ^s is the driving force for the plastic rate which is directly derived from a $\dot{\gamma}^s(\tau^s)$ relationship via a Norton law and two viscosity parameters (here $10\,\mathrm{MPa\,s}^{1/n}$ and $n = 25$ were used).

For each grain, the mean orientation given by the DCT is taken into account for the computations. For the elastic part, an isotropic law was used with a Young Modulus of 83 GPa and a Poisson coefficient of 0.3. For the non-linear material integration, a second order Runge–Kutta time integration scheme with automatic time stepping was used. The lower face of the sample was fully constrained, and a vertical displacement of 180 μm (along the $\underline{z}$ direction) was applied to the upper face, leading to an overall deformation of 12%. The total computation time, using a 32 core machine for multi-threaded material point integration (but still using a non-parallel resolution of the linear system for material equilibrium) was about 60 h.

4.3. Results

Results of the crystal plasticity calculation are summarized in Figure 9. To quantify lattice rotations, the angle ϕ_c associated with the orthogonal matrix $\mathbf{R}^e$ is presented as a function of the evolving deformation in Figure 9 after averaging each grain. The error bars are used to represent the orientation spread in the considered grain as the deformation proceeds.

All three grains experience a non-linear evolution of the rotation angle ϕ_c with a different amplitude in each grain. The error bars shown on Figure 9a, representing the lattice orientation distribution, also increase from 0 to more than 1°. It is interesting to see that grain 18 which undergoes the highest deformation has both the largest rotation and the largest orientation spread.

The grain reorientations can also be plotted using an inverse pole figure which shows how the $\underline{z}$ direction changes with respect to the crystal lattice (see Figure 9b). In this case, the expression of the loading axis in the deformed crystal frame is obtained by $^t\mathbf{R}^e \cdot \mathbf{B} \cdot \underline{z}$.

5. Conclusions

Crystal plasticity full field calculations provide a wealth of information which could be compared to experimental measurements. In this paper we have shown how to turn 3D experimental grain maps into a FE mesh suitable for mechanical analysis. The global specimen behavior can then be
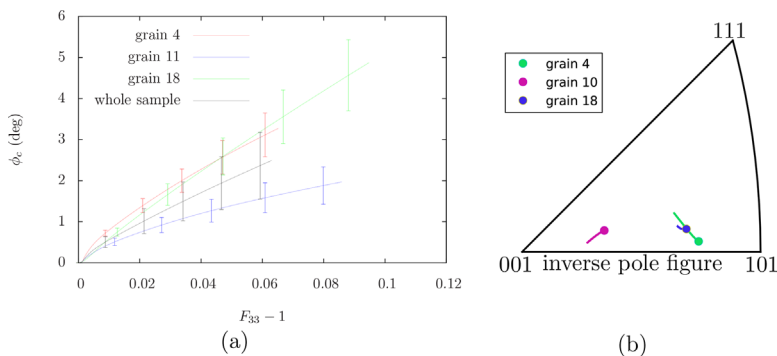

(a) (b)

Fig. 9. (a) Evolution of mean lattice rotations and orientation spread (see error bars) during the specimen deformation; (b) inverse pole figure showing the evolution of the loading axis in the crystal lattice of the three grains (the large dot correspond to the initial orientation).

predicted but more interestingly, the prediction of the average lattice rotation can be achieved for each grain. Intra grain lattice rotation are also readily available and can be compared to the orientation maps from HEDM[40] or 6D-DCT in the future.[11]

Prescribing accurate boundary conditions is essential to achieve precise estimations of average stress or strain tensors in microstructral grains but are difficult to know precisely in 3D. If possible (for instance if the specimen microstructure provides a natural speckle thanks to small porosities or second phase particles), one should carry out digital volume correlation on absorption contrast tomography images during the test. At least some small markers should be attached to the sample to verify the applied loading conditions.

Complete studies require to chain a rather high number of computational tools which are still under development although some of them have matured a lot in the last 5 years. In addition, this methodology usually requires a large amount of computer power to provide local mechanical variables.

In summary, turning experimental 3D microstructures into input for FE calculations is a promising way forward to complement the rising 3D techniques related to polycrystalline materials. It may provide complete mesoscale informations to study deformation and fracture of structural materials in the near future.

[1] C. Teodosiu, *Large Plastic Deformation of Crystalline Aggregates*, CISM Courses and Lectures No. 376, Udine, Springer Verlag, Berlin **1997**.

[2] E. Héripré, M. Dexet, J. Crépin, L. Gélébart, A. Roos, M. Bornert, D. Caldemaison, *Int. J. Plast.* **2007**, *23*, 1512.

[3] C. Maurice, R. Fortunier, *J. Microsc.* **2008**, *230*, 520.

[4] T. B. Britton, J. Jiang, R. Clough, E. Tarleton, A. I. Kirkland, A. J. Wilkinson, *Ultramicroscopy* **2013**, *135*, 126.

[5] T. B. Britton, J. Jiang, R. Clough, E. Tarleton, A. I. Kirkland, A. J. Wilkinson, *Ultramicroscopy* **2013**, *135*, 136.

[6] O. Robach, J.-S. Micha, O. Ulrich, P. Gergaud, *J. Appl. Crystallogr.* **2011**, *44*, 688.

[7] F. Barbe, L. Decker, D. Jeulin, G. Cailletaud, *Int. J. Plast.* **2001**, *17*, 513.

[8] F. Barbe, S. Forest, G. Cailletaud, *Int. J. Plast.* **2001** *17*, 537.

[9] A. Zeghadi, S. Forest, A.-F. Gourgues, O. Bouaziz, *Philos. Mag.* **2007**, *87*, 1425.

[10] R. M. Suter, D. Hennessy, C. Xiao, U. Lienert, *Rev. Sci. Instrum.* **2006**, *77*, 123905.

[11] N. Viganò, W. Ludwig, K. J. Batenburg, *J. Appl. Crystallogr.* **2014**, *47*, 1826.

[12] M. P. Echlin, A. Mottura, C. J. Torbet, T. M. Pollock, *Rev. Sci. Instrum.* **2012**, *83*, 023701.

[13] M. Kremer, D. Bommes, I. Lim, L. Kobbelt, Advanced Automatic Hexahedral Mesh Generation from Surface Quad Meshes. In *Proceedings of the 22nd International Meshing Roundtable*, Springer-Verlag, Berlin, United States **2013**.

[14] L. Signor, P. Villechaise, T. Ghidossi, E. Lacoste, M. Gueguen, S. Courtin, *Mater. Sci. Eng. A* **2016**, *649*, 239.

[15] Y. Guilhem, S. Basseville, F. Curtit, J.-M. Stéphan, G. Cailletaud, *Computat. Mater. Sci.* **2013**, *70*, 150.

[16] A. D. Rollett, R. A. Lebensohn, M. Groeber, Y. Choi, J. Li, G. S. Rohrer, *Modell. Simul. Mater. Sci. Eng.* **2010**, *18*, 074005.

[17] N. Vaxelaire, H. Proudhon, S. Labat, C. Kirchlechner, J. Keckes, V. Jacques, S. Ravy, S. Forest, O. Thomas, *New J. Phys.* **2010**, *12*, 035018.

[18] N. Vaxelaire, S. Labat, T. W. Cornelius, C. Kirchlechner, J. Keckes, T. Schulli, O. Thomas, *Acta Mater.* **2014**, *78*, 46.

[19] A. Groeber, A. Jackson, *Integrating Mater. Manuf. Innovation* **2014**, *3*.

[20] Avizo. http://www.vsg3d.com/avizo, version 7.

[21] Simpleware. http://www.simpleware.com.

[22] F. N'Guyen, *Morphologie mathématique appliquée au développement d'outils de maillage EF automatique dans le cas de microstructures hétérogènes bi et multiphasées*. PhD thesis, Université de Lille 1, **2014**.

[23] E. Roux, M. Bernacki, P. O. Bouchard, *Comput. Mater. Sci.* **2011**, *68*, 32.

[24] M. Bernacki, Y. Chastel, T. Coupez, R. E. Logé, *Scripta Mater.* **2008**, *58*, 1129.

[25] M. Bernacki, R. E. Logé, T. Coupez, *Scripta Mater.* **2011** *64*, 525.

[26] R. Quey, P. R. Dawson, F. Barbe, *Comput. Methods Appl. Mech. Eng.* **2011**, *200*, 1729.

[27] Ziji Wu, J. M. Sullivan Jr, *Int. J. Numer. Methods Eng.* **2003**, *58*, 189.

[28] A. Guéziec, Surface Simplification Inside a Tolerance Volume. *Technical Report RC 20440*, IBM Research Center, Yorktown Heights NY, United States, **1997**.

[29] Ghs3d. https://www.rocq.inria.fr/gamma/gamma/ghs3d, version 3. 2–3.

[30] P. L. George, H. Borouchaki, Triangulation de Delaunay et maillage: Application aux éléments finis. Editions HERMES, *Paris* **1997**.

[31] W. Ludwig, A. King, P. Reischig, M. Herbig, E. M. Lauridsen, S. Schmidt, H. Proudhon, S. Forest, P. Cloetens, S. Rolland du Roscoat, J. Y. Buffière, T. J. Marrow, H. F. Poulsen, *Mater. Sci. Eng. A* **2009**, *524*, 69. Special Topic Section: Probing Strains and Dislocation Gradients with Diffraction.

[32] G. Lutjering, J. C. Williams, *Engineering Materials and Processes, Titanium*, 2nd Edition, Springer, Berlin **2007**.

[33] G. Simmons, H. Wang, *Single Crystal Elastic Constants and Calculated Aggregate Properties: A Handbook*, The MIT Press, Cambridge MA, United States **1971**.

FULL PAPER

[34] A. Cazzani, M. Rovati, *Int. J. Solids Struct*. **2003**, *40*, 1713.

[35] P. Reischig, A. King, L. Nervo, N. Viganó, Y. Guilhem, W. J. Palenstijn, K. J. Batenburg, M. Preuss, W. Ludwig, *J. Appl. Crystallogr*. **2013**, 46297.

[36] R. Becker, S. Panchanadeeswaran, *Textures and Microstruct*. **1989**, *10*, 167.

[37] J. Besson, R. Foerch, *Revue Européenne des Eléments Finis* **1998**, *7*, 535.

[38] J. Besson, G. Cailletaud, J.-L. Chaboche, S. Forest, M. Blétry, *Non-Linear Mechanics of Materials*, Springer, Netherlands **2010**.

[39] J. Mandel, *Int. J. Solids Struct*. **1973**, *9*, 725

[40] J. C. Schuren, P. A. Shade, J. V. Bernier, S. F. Li, B. Blank, J. Lind, P. Kenesei, U. Lienert, R. M. Suter, T. J. Turner, D. M. Dimiduk, J. Almer, *Curr. Opin. Solid State Mater. Sci.* **2015**, *19*, 235.